Modeling the Performance of Direct-Detection Doppler Lidar Systems in Real Atmospheres

Matthew J. McGill*, William D. Hart#, Jack A. McKay@,
and James D. Spinhirne*

Submitted to Applied Optics
March 1999

*NASA Goddard Space Flight Center
Laboratory for Atmospheres, Code 912
Greenbelt, MD 20771
Email: mcgill@virl.gsfc.nasa.gov

#Science Systems Applications, Inc.
Lanham, MD 20706

@Remote Sensor Concepts
Washington, D.C. 20010

ABSTRACT

Previous modeling of the performance of spaceborne direct-detection Doppler lidar systems has assumed extremely idealized atmospheric models. Here we develop a technique for modeling the performance of these systems in a more realistic atmosphere, based on actual airborne lidar observations. The resulting atmospheric model contains cloud and aerosol variability that is absent in other simulations of spaceborne Doppler lidar instruments. To produce a realistic simulation of daytime performance, we include solar radiance values that are based on actual measurements and are allowed to vary as the viewing scene changes. Simulations are performed for two types of direct-detection Doppler lidar systems: the double-edge and the multi-channel techniques. Both systems were optimized to measure winds from Rayleigh backscatter at 355 nm. Simulations show that the measurement uncertainty during daytime is degraded by only about 10-20% compared to nighttime performance, provided a proper solar filter is included in the instrument design.

1. Introduction

Global wind measurements are necessary to improve the understanding and forecasting of weather events. Tropospheric wind speed profile data are important inputs to meteorological models[1] but are generally available only over populated areas where rawindsonde systems or Doppler radar profilers are in operation. A satellite instrument for measuring wind speed profiles would provide data over remote, unpopulated regions of the globe, in particular the oceans of the Southern Hemisphere where data are currently extremely sparse. Important science issues such as the phenomenology of El Nino events, transport of aerosols and water vapor, and atmospheric dynamics can also be addressed through global measurements of the wind field.[2]

Interest in a satellite based laser wind sounder has recently been revived, due to advances in instrument technology. Coherent detection lidar is well established as a ground based and airborne measurement technique,[3] but depends on atmospheric aerosols for infrared backscatter, and may have difficulty over the areas where wind data are most sparse. Direct detection lidar, based on optical measurements of the Doppler shift, is also under study and has the advantage that Rayleigh (molecular) backscatter can be used, permitting measurements under any aerosol conditions.

The potential for building a spaceborne Doppler lidar system necessarily leads to a requirement for predicting on-orbit instrument

performance. Perhaps the most important problem in development of a direct-detection Doppler lidar (DDDL) for spaceflight is the achievement of sufficient accuracy to meet the requirements of the users. Because of the enormous range from the satellite to the point of observation, the small backscatter coefficient of clean air, and the limited dwell time permitted by a fast-moving satellite, it is difficult to acquire sufficient signal to achieve measurement accuracies of less than 1 m/s.

Some modeling of DDDL systems has been done using generalized signal levels[4,5,6,7] that could be extrapolated to spaceborne situations. Various researchers have modeled the performance of spaceborne direct-detection lidar[8,9,10,11] but the calculations have invariably assumed highly idealized atmospheres with fixed aerosol profiles and no clouds. In practice, a DDDL will synthesize a single wind profile measurement from the summation of several hundred laser pulses, across a ground track 100 to 200 km long. The measurement will necessarily involve atmospheric aerosol profiles varying substantially along the measurement track. Furthermore, since clouds are to be expected on a large proportion of the shots, the effects of clouds on the measurement cannot be ignored.

Here we describe a first effort to develop a technique for more realistic simulations of the operation of a DDDL, including the effects of aerosol and cloud variability. The initial objective is to determine the consequences of a more realistic atmosphere, thereby allowing us to develop better predictions of the on-orbit performance of potential systems. This initial assessment will consider the two principal candidates for the DDDL, namely the multi-channel (or fringe imaging) system,[12,13,14,15] and the double-edge

technique[16,17,18], to determine whether one method or the other will be especially strongly affected by clouds, or by variable aerosol profiles. We include in the system models an optimized solar prefilter and we synthesize solar radiance data based on measured albedo values. We have previously shown that the two DDDL methods produce equivalent results for idealized aerosol and molecular signals.[6] In this work we will determine if there will be differences for a more realistic atmosphere.

The investigation has been based on a specific, real set of atmospheric cloud and aerosol data obtained from the Cloud Lidar System (CLS) developed by Spinhirne et al.[19] The results therefore will pertain to this particular set of conditions. In time, the work will be generalized to other atmospheric conditions. This preliminary work will yield a first look at the consequences of a real atmosphere on the accuracy of potential DDDL systems, in daylight and in darkness.

2. Doppler lidar receiver models

The direct-detection Doppler lidar technique relies on directly sensing the wavelength shift of atmosphere-backscattered light relative to the wavelength of the outgoing laser light. Models for the estimation of the accuracy of DDDL systems have recently been published by McGill and Spinhirne[5]. That work provides analyses of the measurement accuracy of multi-channel (MC) systems, and of double-edge (DEDG) instruments. Those receiver models, along with sets of practical instrument parameters, will be used here to simulate the performance of spaceborne DDDL systems.

It has already been shown that these two Doppler lidar techniques yield essentially the same measurement accuracy when using idealized atmospheres.[5,6,7] Now we wish to determine how the two techniques will compare when presented with a more realistic target atmosphere.

The DEDG method[16,17,18] uses two Fabry-Perot interferometers (or etalons), identical except for the center frequencies, that are symmetrically located about the laser frequency. The etalon may be a single physical unit, with the optical gap made slightly different for two halves of the aperture.[16] Doppler shifts cause the transmitted signal to increase on one etalon while simultaneously decreasing on the second etalon. The incident photons are divided, with about half going into each etalon. The output of each etalon is measured separately on single element detectors and Doppler shifts are determined from changes in the measured transmitted signal of the two filters.

The MC method[12,13,14,15] differs from the DEDG method by using an imaging (i.e., multiple element) detector. A Fabry-Perot etalon modulates the return signal with its transmittance function, forming an interference fringe on the detector. While the DEDG method measures the output of each etalon on a single detector the MC method divides the etalon output into several "channels", or wavelength intervals, to allow full resolution of the spectrum. The photocounts on each channel are measured simultaneously and independently. The Doppler shift is inferred by measuring the angular displacement of the centroid of the backscattered signal compared to the center wavelength of the outgoing laser shape.[14]

A complete description of the predictive and error equations can be found in Ref. 5. For reference, the pertinent equations are repeated in Appendix A. As shown by McGill and Spinhirne[5], the error equation for

the DEDG system is a special case of the MC equation. The uncertainty in the horizontal wind component, σU_H, for both of these direct-detection systems can be written as:

$$\sigma_{U_H} = \sqrt{\frac{c^2}{4\lambda^2 \sin^2\phi \sum_{j=1}^{n_c}\left[SNR^2(j)\left(\frac{1}{N(j)}\frac{\partial N(j)}{\partial \lambda}\right)^2\right]}} \quad . \tag{1}$$

where SNR is the signal-to-noise ratio on each detector element, j, N is the number of photons detected on each detector, ϕ is the observation zenith angle, λ is the laser wavelength, and c is the speed of light.

DDDL systems can be designed to measure winds using either the narrow aerosol backscattered spectrum (~100 MHz FWHH) or the wider signature of Rayleigh backscatter (~3.5 Hz FWHH). For this work we focus only on receivers optimized to measure Doppler shifts from the Rayleigh backscatter at 355 nm.

A spaceborne DDDL will sum multiple pulses along the flight track to accumulate sufficient signal for high measurement accuracy. In the example used here, the spacecraft operates in a step-stare scan pattern such that the lidar wind measurements are obtained by summing 350 laser pulses along a 27 km path. We assume the signals are summed and the integrated signal is processed, as opposed to processing each pulse and combining the results. Thus, the variable N(j) in Eqn. 1 (and in Appendix A) represents the sum of the signal photons plus any solar or noise photons over 350 laser pulses.

3. Cloud Lidar System aerosol measurements

The CLS measures profiles of attenuated backscatter at 532 nm and 1064 nm.[19,20] The CLS flies on an ER-2 aircraft at altitudes as high as 20 km. Because these flights are above virtually all atmospheric aerosols and clouds, the lidar profiles will be good models for a spaceflight DDDL.

For this work we will focus on the 1064 nm data because a greater range of these data sets have already been analyzed and are available for further modification as described here. The procedures for processing the raw instrument data are well documented.[20,21,22] The CLS data are processed to identify cloud boundaries, with a procedure allowing identification of up to five cloud layers per profile. Boundaries of clouds are found in each of the profiles by comparing the profile signal to a threshold developed from independent investigation.

Figure 1 shows an example of the CLS data acquired over the tropical Pacific during the TOGA/COARE campaign on January 7, 1993. This data set will be employed here to develop and illustrate the procedures for using these data for satellite DDDL simulation. In future work, CLS data from other regions will be evaluated for assessment of DDDL performance under a variety of atmospheric conditions.

The data of Figure 1 include large areas of dense cloud cover, as is typical of the Intertropical Convergence Zone. Cloud cover is a significant issue for active remote sensing instruments, because measurements are not possible through optically thick clouds and because clouds are high-albedo sunlight reflectors, potentially degrading the lidar Doppler measurement. We caution that the CLS data cannot be considered as a global climatology for the cloud cover. However, our purpose here is to

generate a small-scale simulation of a spaceborne Doppler lidar while developing the computational tools that will permit future simulations using global-scale data sets.

The CLS fundamentally acquires profiles of attenuated backscatter. However, DDDLs respond differently to aerosol and Rayleigh backscatter, so the two components must be extracted from the CLS data. For this work, an algorithm published by Spinhirne et al.[23] was used to convert the CLS attenuated backscatter profiles to aerosol backscatter coefficients. The conversion requires two assumptions. First, we assume a Rayleigh backscatter profile as shown in Figure 2.[24] Second, we must assume an extinction-to-backscatter ratio for the aerosol scattering. An extinction-to-backscatter ratio of 18 sr is used for clouds below 9 km (presumed water clouds)[25] and a ratio of 30 sr for clouds above 9 km[21] (appropriate for cirrus clouds). For cloud-free regions, a ratio of 30 sr is assumed for the boundary layer (<3 km), and 45 sr for altitudes greater than 3 km.[26] Other conversion parameters might be chosen, but the effects on the aerosol backscatter coefficients will be modest, and the consequences for the DDDL modeling will be small.

The DDDL modeling will assume operation at 355 nm, i.e., frequency tripled Nd:YAG, as is appropriate for a Rayleigh backscatter DDDL. A simple λ^{-1} scaling is chosen to scale the aerosol backscatter coefficients to 355 nm, except for clouds, which are assumed to have backscatter coefficients independent of wavelength. The result of converting from profiles of attenuated backscatter at 1064 nm to aerosol backscatter coefficient at 355 nm is shown in Figure 3. Although the CLS data starts at 20 km, we have omitted the first three kilometers to avoid any telescope overlap or aircraft-induced effects.

The spatial resolution of the raw CLS profiles is 7.5 m vertical by 200 m horizontal at zero degrees zenith. The spatial values are combined to simulate a spaceborne system with a vertical spatial resolution of 1 km, with individual laser pulses separated by 77 m, corresponding to a 100 Hz laser in a 400 km orbit operating at a 30 degree zenith angle. This procedure yields profiles of aerosol and Rayleigh backscatter as would be seen by a satellite DDDL traversing the path followed by the CLS ER-2. While certainly not representative of the entire globe, this example will be illustrative of a situation that will be encountered by an operational satellite lidar system. We also defined a model wind profile, shown in Figure 4, based on suggested parameters of Emmitt et al.[27] The wind profile is taken to be constant across the distance of one wind profile measurement.

4. The Solar Background

A critical problem for direct-detection is the solar background. The downward-looking DDDL will see sunlight reflected from high-albedo clouds, producing a strong background signal that will interfere with the lidar return. We assume that this background signal can be accurately measured (e.g., by reading the detector levels between laser pulses) and subtracted from the signal plus background readings. Assuming that the background level does not change between the time of the background measurement and the lidar signal measurement, the only effect on the measurement is the shot noise of the solar background. This background shot noise is incorporated in the measurement uncertainty models.

For this work the solar spectral irradiance at 355 nm at the top of the atmosphere is taken to be 0.9 W/(m^2-nm) [28]. Albedo values at 355 nm were

obtained from the Global Ozone Monitoring Experiment (GOME).[29] Based on the GOME data we assign albedo values of 0.23 for clear sky and 0.65 for a cloudy sky. Atmospheric attenuation in the ultraviolet reduces the effective albedo of tropospheric clouds by an amount that will depend on the cloud altitude. By estimating this attenuation factor for different altitudes, we compiled a table of radiance values for differing cloud conditions (Table 1). These various radiance values can then be matched to each of the CLS profiles, providing estimates of the highly variable solar background that would be seen by a satellite lidar.

To simulate a receiver system for daytime operation requires that the Doppler analyzer model include an optimized filter arrangement. Besides the spectral resolving etalon, a spaceborne system will require additional filtering elements to suppress solar background. Instrument design studies[11,30,31] have shown that a practical spaceborne DDDL with a large telescope field of view must utilize a triple etalon configuration, similar to the HRDI Doppler analyzer[32] for operation in daylight. In this study we assume a 200 μradian (full angle) receiver field of view. Laser-receiver alignment error estimates for actual spaceflight systems range from 150 μradians to 375 μradians, so an assumption of a much smaller field of view to obviate the multiple etalon solar filter would not be plausible. We find the best instrument performance will be achieved when the high-resolution spectral resolving etalon (hereafter HRE) is operated in tandem with a wide-band dielectric filter (DF), a low resolution etalon (LRE), and a medium resolution etalon (MRE).

Tandem-etalon solar filter designs were developed separately for the MC and DEDG Doppler receivers, using design procedures developed by McKay .[31] Both begin with a dielectric filter with 0.2 nm passband width,

representing the current state of the art of multilayer dielectric filter technology. Absorbers with 5% attenuation between each etalon pair were included to reduce the effects of reflective coupling between the etalons.[28] The LRE and MRE of the two designs differ slightly, due to the difference in HRE free spectral range. The overall signal transmittance of the two solar filter etalons and two absorbers is 74%. The transmittance of the dielectric filter is included in the optical efficiency of the system separately from the tandem etalon solar filter.

The best etalon plates have surface imperfections on the order of $\lambda/200$, where λ here is the characterization wavelength of 633 nm. The defect finesse corresponding to this plate smoothness is about 43.[33] The defect finesse scales as λ, so the value at 355 nm will be about 24. The reflectance finesse must be less than this to yield high signal transmittance. Here a reflectance finesse of 10.4 is assumed, corresponding to an etalon peak transmittance of 90%, and an effective finesse of 9.5.

Numerical integration across the full bandwidth of the dielectric filter yields the integrated transmittance of the filter system for white-light illumination. This is stated as the effective passband width of an idealized, square-passband filter with in-band transmittance equal to the peak transmittance of the two solar filter etalons and two absorbers. In the case of the MC system, the effective bandwidth is 3.65 pm, while for the DEDG, which has smaller etalon gap increments, the bandwidth is 2.66 pm. Thus it happens that the DEDG receiver will benefit from a solar filter with slightly higher performance than that of the MC receiver.

5. Applying the Doppler receiver models to CLS data

DDDL systems can be designed to measure winds using either the narrow aerosol backscattered spectrum (~100 MHz FWHH) or the wider signature of Rayleigh backscatter (~3.5 GHz FWHH at 355 nm). The former backscatter signal yields higher accuracy per backscattered photon, but regions of the atmosphere with low aerosol density will produce few signal photons. The Rayleigh signal requires much stronger returns to obtain high accuracy, but is universally available. The ubiquity of the Rayleigh return is the principal advantage of direct detection, versus coherent, and for this work we focus only on receivers optimized to measure Doppler shifts from the Rayleigh backscatter at 355 nm.

The simulations require assumption of instrument parameters. General parameters for the spacecraft system are listed in Table 2. In Table 3 we list the parameters specific to the two DDDL systems. These parameters have been chosen to yield optimal performance for each Doppler analyzer.

Applying the Doppler receiver models to the CLS-derived atmosphere yields the results shown in Figure 5 for the MC receiver and Figure 6 for the DEDG receiver. Figures 5(a) and 6(a) are for a nighttime system (i.e., including no background signals). Figures 5(b) and 6(b) include solar background as defined by Table 1. The errors shown are line-of-sight uncertainty. To convert to error in the horizontal component of the vector wind requires dividing the line-of-sight error by sin ϕ, as shown in Eqn. 1.

For the receiver systems defined here, the DEDG receiver in the free troposphere performs slightly better in darkness than the MC receiver by a factor of 1.10. This is due to slightly higher measurement sensitivity for the

DEDG system. However, the advantage of one system relative to the other is very small and is consistent with the results of McGill and Spinhirne,[5] and of McKay,[6,7] that there is no large difference in measurement sensitivity between the two techniques.

In the cloud-free regions (as at 1000-1500 km distance along track), the presence of solar background increases the measurement uncertainty by a factor of 1.04 for the MC receiver and 1.07 for the DEDG receiver. In regions above high thins clouds (as at 50 km along-track distance) the degradation is a factor 1.06 for the MC receiver and 1.14 for the DEDG receiver. In regions above high bright clouds (as at 2500-3000 km along-track distance) the degradation is a factor 1.10 for the MC receiver and 1.19 for the DEDG receiver. In general, we find that the DEDG system is more strongly affected by the background sunlight than the MC system, despite the better solar filter performance. This is due to the signal division and weighting that occurs for the MC system (see Eqn. 1). For the MC system the solar signal is divided across all detector elements which are then weighted according to the signal-to-noise ratio, thereby effectively reducing the impact of solar background. We point out, however, that for neither of these DDDL receivers is the measurement uncertainty significantly degraded by the solar background.

In regions with high aerosol content (e.g., the planetary boundary layer), the MC receiver performs substantially better than the DEDG. The narrow spectral linewidth of the aerosol return yields high measurement accuracy per backscattered photon for the MC Doppler analyzer. The MC analyzer measures the Doppler shift by the physical displacement of the signal across the imaging detector, and the displacement of the aerosol signal, per unit Doppler shift, is the same as the displacement of the

Rayleigh signal. Hence the MC analyzer can make full use of the aerosol signal when it is present. The DEDG Doppler analyzer, by converting the Doppler shift to amplitudes, has in general very different sensitivities to the aerosol and Rayleigh signals. This characteristic must be suppressed for unambiguous measurement of the Doppler shift. For this purpose, the DEDG is operated at a condition which reduces the sensitivity to the aerosol signal to match the sensitivity to the Rayleigh signal.[17,34] This desensitizes the DEDG to the aerosol signal, so it does not much benefit from the presence of a strong aerosol component.

6. Conclusion

Previous modeling of the performance of direct-detection Doppler lidar systems has assumed extremely idealized atmospheric models, consisting of single, constant aerosol profiles and cloud-free atmospheres. Here we have developed a technique for modeling the performance of these systems in a more realistic atmosphere, based on actual airborne lidar observations across thousand-kilometer tracks. The resulting atmospheric model contains cloud and aerosol variability that is absent in other simulations of spaceborne Doppler lidar instruments.

To further provide a realistic simulation of spaceborne performance, we included solar radiance values that are based on actual measurements and are allowed to vary as the viewing scene changes. The result is an accurate and realistic simulation of the daytime performance of a spaceborne Doppler lidar. Simulations were performed for two types of direct-detection Doppler lidar systems: the double-edge and the multi-

channel techniques. Both systems were optimized to measure winds from Rayleigh backscatter at 355 nm.

Simulations for daytime and nighttime conditions show that for neither of the two systems was the measurement uncertainty severely degraded by solar background, provided a tandem etalon solar filter is included in the instrument design. The degradation of the measurement uncertainty during daytime is only about 10-20% compared to the nighttime performance. The DEDG system is slightly more affected by the solar background than the MC receiver, a result that could be significant if the solar filtering is not as effective as assumed here, or if lower power systems are assumed. For laser power less than the 32 W assumed here, the solar background would be more significant.

The simulations further show that the MC system benefits more from atmospheric aerosols, when present, that the DEDG system. The DEDG system is designed specifically to reduce its sensitivity to the aerosol signal, since otherwise the technique becomes unusable in regions of mixed signal. Hence it does not benefit significantly from the aerosol component of the backscatter signal. The MC system is not bothered by the mixed atmosphere signal and benefits from higher sensitivity to the aerosol component of the backscatter signal.

Appendix A

One of the primary conclusions of McGill and Spinhirne[5] was that the DEDG concept was a special case of the MC method and hence similar equations apply to both methods. In this appendix we briefly review the equation for calculating the number of photons measured by a direct-detection lidar. The equation for determining the error in the wind measurement is given in Eqn. 1.

For either type of DDDL receiver, the number of signal photons, N_S, detected on each detector element, j, is given by:

$$N(j) = \kappa\varepsilon Q_E(j)\sum_{n=0}^{\infty}\mathcal{A}_n \mathrm{sinc}\left(\frac{n}{\mathcal{F}_A}\right) e^{-\pi^2 n^2 \Delta\lambda_L^2/\Delta\lambda_{FSR}^2}\left(\alpha + \omega\, e^{-\pi^2 n^2 \Delta\lambda_M^2/\Delta\lambda_{FSR}^2}\right) \tag{A1}$$

$$\times \cos\left[2\pi n\left(\xi - \frac{2U_H\lambda_L \sin\phi}{c\Delta\lambda_{FSR}}\right)\right]$$

where $Q_E(j)$ is the detector quantum efficiency, $\Delta\lambda_{FSR}$ is the wavelength free spectral range, $\Delta\lambda_L$ is the laser 1/e-width, $\Delta\lambda_M$ is the molecular 1/e-width, λ_L is the laser wavelength, U_H is the horizontal wind velocity, ϕ is the observation zenith angle, the sinc term is an aperture broadening function with $\mathcal{F}_A$ being the aperture finesse, and κ, α and ω are defined below. $\mathcal{A}_n$ is defined as

$$\mathcal{A}_n = \left(1 - \frac{\mathcal{L}}{1-\mathcal{R}}\right)^2\left(\frac{1-\mathcal{R}}{1+\mathcal{R}}\right) \qquad \text{for } n = 0,$$

$$\mathcal{A}_n = 2\left(1-\frac{\mathcal{L}}{1-\mathcal{R}}\right)^2\left(\frac{1-\mathcal{R}}{1+\mathcal{R}}\right)\mathcal{R}^n e^{-4\pi^2 n^2 \Delta d_D^2/\lambda_0^2} \qquad \text{for } n > 0. \tag{A2}$$

where $\mathcal{L}$ accounts for any absorptive or scattering losses in the etalon plates, $\mathcal{R}$ is the plate reflectivity, and Δd_D is an etalon defect parameter.

The terms ε and ξ are different for MC or DEDG receivers. The constant ε describes the division of incident signal according to the number of detector elements:

$$\varepsilon = \begin{cases} 1/n_C & \text{for MC} \\ T_{BS} & \text{for DEDG} \end{cases} \tag{A3}$$

where n_c is the number of detector elements in the MC detector and T_{BS} is a beamsplitter transmission in the DEDG receiver. The parameter ξ describes the offset of the laser line position from the central wavelength of the etalon:

$$\xi = \begin{cases} \dfrac{\lambda_L - \lambda_C}{\Delta\lambda_{FSR}} - \dfrac{j}{N_{FSR}} & \text{for MC} \\ \pm\dfrac{\delta}{2\mathcal{F}_{EFF}} & \text{for DEDG} \end{cases} \tag{A4}$$

where N_{FSR} is the number of detector channels per etalon free spectral range, the term $(\lambda_L - \lambda_C)$ accounts for any offset in the position of the laser line with respect to the central wavelength of the etalon, λ_C, $\mathcal{F}_{EFF}$ is the effective etalon finesse (which includes all broadening effects), and the term $+/-\delta/2\mathcal{F}_{EFF}$ describes the offset of the laser line relative to the etalon with δ being in units of etalon halfwidths.

The terms α and ω are generalized quantities defined as

$$\alpha = P_A(\pi)\beta_A \cdot \exp\left\{-2\int_0^r (\beta_A + \beta_M)dr'\right\} \tag{A5}$$

$$\omega = P_M(\pi)\beta_M \cdot \exp\left\{-2\int_0^r (\beta_A + \beta_M)dr'\right\}, \qquad \text{(A6)}$$

where $P_A(\pi)$ and $P_M(\pi)$ are the aerosol and molecular backscatter phase functions and β_A and β_M are the aerosol and molecular volume scattering coefficients.

The constant κ describes instrument parameters:

$$\kappa = \frac{E_T \lambda}{hc} \frac{A_T}{4\pi} \frac{\Delta r}{r^2} T_O O_A(r) \qquad \text{(A7)}$$

where E_T is the transmitted laser energy, A_T is the telescope area, Δr is the range bin length, r is the distance to the scattering particle, T_O is the system optical efficiency (not including the spectral resolving Fabry-Perot etalon), and $O_A(r)$ describes the transmitter-receiver overlap function.

References

1. R. M. Atlas, "Atmospheric observations and experiments to assess their usefulness in data assimilation," *Journal of the Meteorological Society of Japan*, **75**, 111-130 (1997).

2. W.E. Baker, G.D. Emmitt, F. Robertson, R.M. Atlas, J.E. Molinari, D.A. Bowdle, J. Paegle, R.M. Hardesty, R.T. Menzies, T.N. Krishnamurti, R. A. Brown, M.J. Post, J.R. Anderson, A.C. Lorenc, and J. McElroy, "Lidar-measured winds from space: A key component for weather and climate prediction," *Bulletin of the American Meteorological Society*, **76**, 869-888 (1995).

3. J. Rothermal, D.R. Cutten, R.M. Hardesty, R.T. Menzies, J.N. Howell, S.C. Johnson, D.M. Tratt, L.D. Olivier, and R.M. Banta, "The Multi-center Airborne Coherent Atmospheric Wind Sensor," *Bulletin of the American Meteorological Society*, **79**, 581-599 (1998).

4. B.J. Rye, "Comparative precision of distributed-backscatter Doppler lidars," *Applied Optics*, **34**, 8341-8344 (1995).

5. M.J. McGill and J.D. Spinhirne, "Comparison of two direct-detection Doppler lidar techniques," *Optical Engineering*, **37**, 2675-2686 (1998).

6. J.A. McKay, "Modeling of direct detection Doppler wind lidar: I. The edge technique," *Applied Optics*, **37**, 6480-6486 (1998).

7. J.A. McKay, "Modeling of direct detection Doppler wind lidar: II. The fringe imaging technique," *Applied Optics*, **37**, 6487-6493 (1998).

8. V.J. Abreu, "Wind measurements from an orbital platform using a lidar system with incoherent detection: A n analysis," *Applied Optics*, **18**, 2992-2997 (1979).

9. R.T. Menzies, "Doppler lidar atmospheric wind sensors: A comparative performance evaluation for global measurement applications from earth orbit," *Applied Optics*, **25**, 2546-2552 (1986).

10. D. Rees and I.S. McDermid, "Doppler lidar atmospheric wind sensor: Reevaluation of a 355-nm incoherent Doppler lidar," *Applied Optics*, **29** 4133-4144 (1990).

11. W.R. Skinner and P.B. Hays, "A comparative study of coherent and incoherent Doppler lidar techniques," report to Marshall Space Flight Center, NAS8-38775 (June 1994).

12. V.J. Abreu, J.E. Barnes, and P.B. Hays, "Observations of winds with an incoherent lidar detector," *Applied Opt.ics*, **31**, 4509-4514 (1992).

13. K.W. Fischer, V.J. Abreu, W.R. Skinner, J.E. Barnes, M.J. McGill, and T.D. Irgang, "Visible wavelength Doppler lidar for measurement of wind and aerosol profiles during day and night," *Optical Engineering*, **34**, 499-511 (1995).

14. M.J. McGill, W.R. Skinner, and T.D. Irgang, "Analysis techniques for the recovery of winds and backscatter coefficients from a multiple channel incoherent Doppler lidar," *Applied Optics*, **36**, 1253-1268 (1997).

15. D. Rees, G. Nelke, K.-H. Fricke, U. von Zahn, W. Singer, G. von Cossart, and N.D. Lloyd, "The Doppler wind and temperature system of the Alomar lidar," *Journal of Atmospheric and Terrestrial Physics*, **58**, 1827-1842 (1996).

16. M.L. Chanin, A. Garnier, A. Hauchecorne, and J. Porteneuve, "*A Doppler lidar for measuring winds in the middle atmosphere,*" Geophysical Research Letters, **16**, 1273-1276 (1989).

17. M.L. Chanin, A. Hauchecorne, A. Garnier, and D. Nedeljkovic, "Recent lidar developments to monitor stratosphere-troposphere exhange," *Journal of Atmospheric and Terrestrial Physics*, **56**, 1073-1081 (1994).

18. C.L. Korb, B.M. Gentry, S.X. Li, and C. Flesia, "Theory of the double-edge technique for Doppler lidar wind measurement," *Applied Optics*, **37**, 3097-3104 (1998).

19. J.D. Spinhirne, M.Z. Hansen, and L.O. Caudill, "Cloud top remote sensing by airborne lidar," *Applied Optics*, **22**, 1564-1571 (1982).

20. J.D. Spinhirne and W.D. Hart, "Cirrus structure and radiative parameters from airborne lidar and spectral radiometer observations," *Monthly Weather Review*, **118**, 2329-2343 (1990).

21. J.D. Spinhirne, W.D. Hart, and D.L. Hlavka, "Cirrus infrared parameters and shortwave reflectance relations from observations," *Journal of the Atmospheric Sciences*, **53**, 1438-1458 (1996).

22. R. Boers, J.D. Spinhirne, and W.D. Hart, "Lidar observations of the fine-scale variability of marine stratocumulus clouds," *Journal of Climate and Meteorology*, **28**, 797-810 (1988).

23. J.D. Spinhirne, J.A. Reagan, and B.M. Herman, "Vertical distribution of aerosol extinction cross section and inference of aerosol imaginary index in the troposphere by lidar technique," *Journal of Applied Meteorology*, **19**, 426-438 (1980).

24. R.A. McClatchey, R.W. Fenn, J.E.A. Selby, F.E. Volz, and J.S. Garing, "Optical Properties of the Atmosphere (revised)," Environmental Research Papers, Air Force Cambridge Research Laboratories, AFCRL-71-0279 (1971).

25. R.G. Pinnick, S.G. Jennings, P. Chylek, C. Ham, and W.T. Grandy, "Backscatter and extinction in water clouds," *Journal of Geophysical Research*, **88**, 6787-6796 (1983).

26. J. Ackermann, "The extinction-to-backscatter ratio of tropospheric aerosol: A numerical study," *Journal of Atmospheric and Oceanic Technology*, **15**, 1043-1050 (1998).

27. G.D. Emmitt, J. Spinhirne, R. Menzies, D. Winker, and D. Bowdle, "Target atmospheres for use in DWL concept studies," 4th draft, February 1998. This document can be found at http://cyclone.swa.com/LidarProducts/targetAtm/.

28. L.A. Hall, L.J. Heroux, and H.E. Hinteregger, "Solar Ultraviolet Irradiance," in *Handbook of Geophysics and the Space Environment*, A.S. Jursa, editor, Air Force Geophysics Laboratory, NTIS-ADA-167000, (1985).

29. J.P. Burrows, M. Weber, M. Buchwitz, V. Rozanov, A. Ladstattler-Weissenmayer, A. Richter, R. DeBeek, R. Hoogen, K. Bramstedt, K.-U. Eichmann, M. Eisinger, "The Global Ozone Monitoring Experiment (GOME): Mission concept and first scientific results," *Journal of the Atmospheric Sciences,* **56**, 151-175 (1999).

30. W.R. Skinner, P.B. Hays, and V.J. Abreu, "Optimization of a triple etalon interferometer," *Applied Optics*, **26**, 2817-2827 (1987).

31. J.A. McKay, "Single and tandem Fabry-Perot etalons as solar background filters for lidar," submitted to *Applied Optics*, (AO-15276), January 1999.

32. P.B. Hays, V.J. Abreu, M.E. Dobbs, D.A. Gell, H.J. Grassl, and W.R. Skinner, "The High Resolution Doppler Imager on the Upper Atmosphere Research Satellite," *Journal of Geophysical Research*, **98**, 10713-10723 (1993).

33. G. Hernandez, *Fabry-Perot Interferometers*, Cambridge Studies in Modern Physics, Cambridge University Press, New York (1986).

34. C. Flesia and C.L. Korb, "Theory of the double-edge molecular technique for Doppler lidar wind measurement," *Applied Optics*, **38**, 432-440 (1999).

Table 1: Spectral radiance values for differing clouds conditions.

CLOUD ALTITUDE	GROUND SEEN?	SPECTRAL RADIANCE [W/(m²*nm*sr)]
Clear sky	Yes	0.051
> 10 km	Yes	0.081
> 10 km	No	0.132
> 7 km, < 10 km	No	0.122
> 4 km, < 7 km	No	0.111
< 4 km	No	0.091

Table 2: Parameters for spacecraft system.

PARAMETER	VALUE
laser 1/e-width ($\Delta\lambda_L$)	2.25×10^{-5} nm (53.6 MHz)
molecular 1/e-width ($\Delta\lambda_M$)	9.67×10^{-4} nm (2.30 GHz)
satellite altitude	400 km
zenith angle	30 degrees
scan pattern	step-stare
telescope aperture	1.25 m
telescope field of view (full angle)	200 μrad
vertical resolution	1 km
horizontal resolution	200 km
laser power	320 mJ/pulse at 100 Hz
integrated laser energy per L-O-S measurement	112 J

Table 3: Parameters for MC and DEDG Rayleigh receivers.

	DEDG SYSTEM	MC SYSTEM
HRE spacing (d)	1.25 cm	1.8 cm
HRE plate reflectivity ($\mathcal{R}$)	75.2%	66%
HRE reflective finesse ($\mathcal{F}_R$)	10.98	7.51
HRE etalon defect (Δd_D)	3.15 nm	3.15 nm
HRE defect finesse	24	24
HRE aperture finesse ($\mathcal{F}_A$)	9.27	32.
HRE effective finesse ($\mathcal{F}_{EFF}$)	6.84	7.20
loss per plate ($\mathcal{L}$)	0.2%	0.2%
HRE free spectral range ($\Delta\lambda_{FSR}$)	5.04×10^{-3} nm (12.0 GHz)	3.5×10^{-3} nm (8.33 GHz)
transmission of absorber between HRE-MRE	95%	95%
MRE spacing	1.92 mm	2.12 mm
MRE reflectivity	74%	74%
MRE defect finesse	24	24
transmission of absorber between MRE-LRE	95%	95%
LRE spacing	0.296 mm	0.249 mm
LRE reflectivity	74%	74%
LRE defect finesse	24	24
dielectric filter (DF) FWHH	0.2 nm	0.2 nm
optical efficiency (includes DF, but not etalons)	34%	34%

filter efficiency (LRE, MRE, absorbers)	74%	74%
overall optical efficiency (T_o)	25.2%	25.2%
integrated solar bandpass	2.66 pm	3.65 nm
detector channels (n_C)	------	32
# orders imaged	------	1.
offset in etalon HWHH	3.10 (2.72 GHz)	-----
detector efficiency (Q_E)	40%	40%

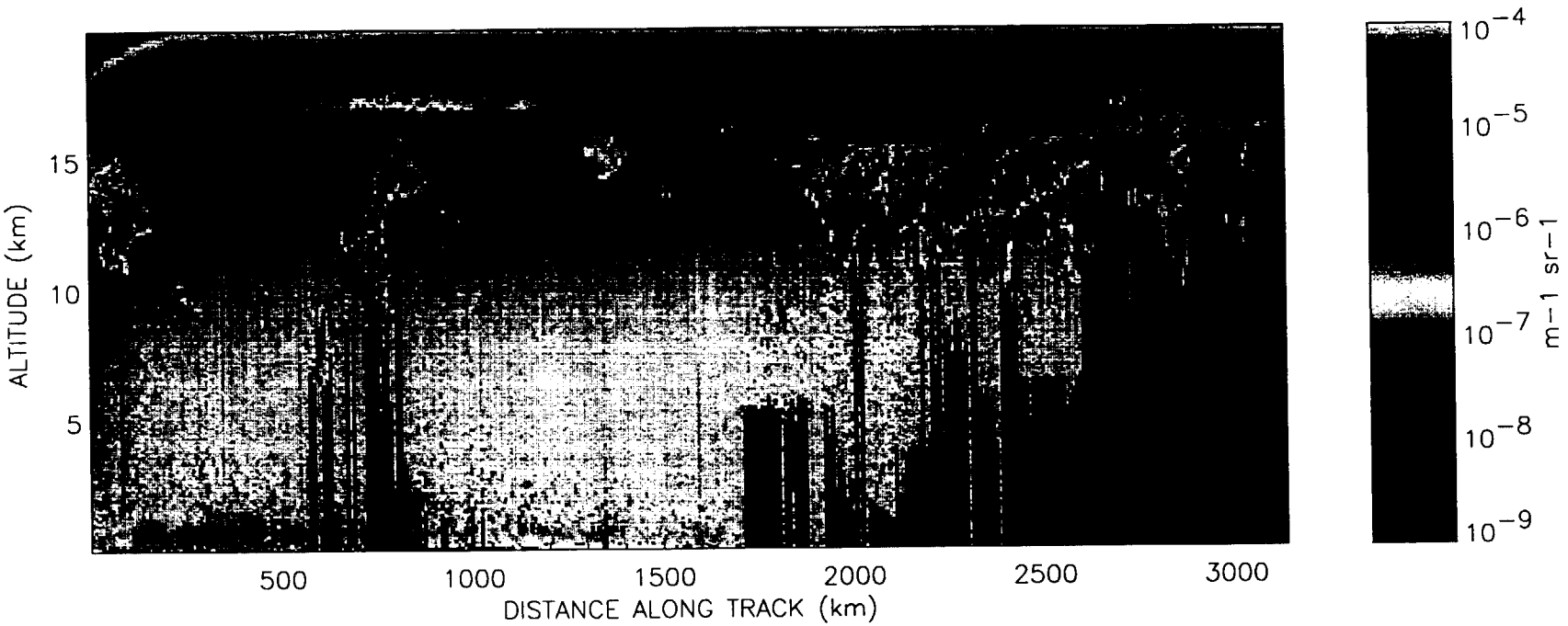
ALTITUDE (km)
15
10
5
500
1000
1500
2000
2500
3000
DISTANCE ALONG TRACK (km)
10^{-4}
10^{-5}
10^{-6}
10^{-7}
10^{-8}
10^{-9}
m−1 sr−1

Fig 1

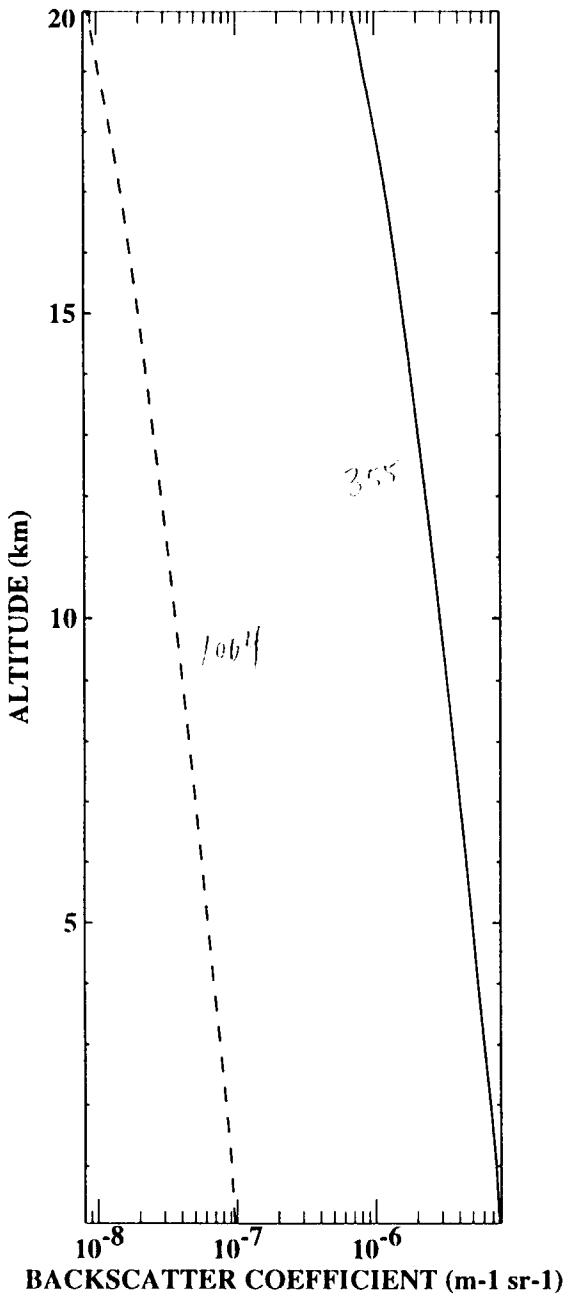
20
15
10
5
ALTITUDE (km)
355
1064
10^{-8}
10^{-7}
10^{-6}
BACKSCATTER COEFFICIENT (m-1 sr-1)

FIG 2.

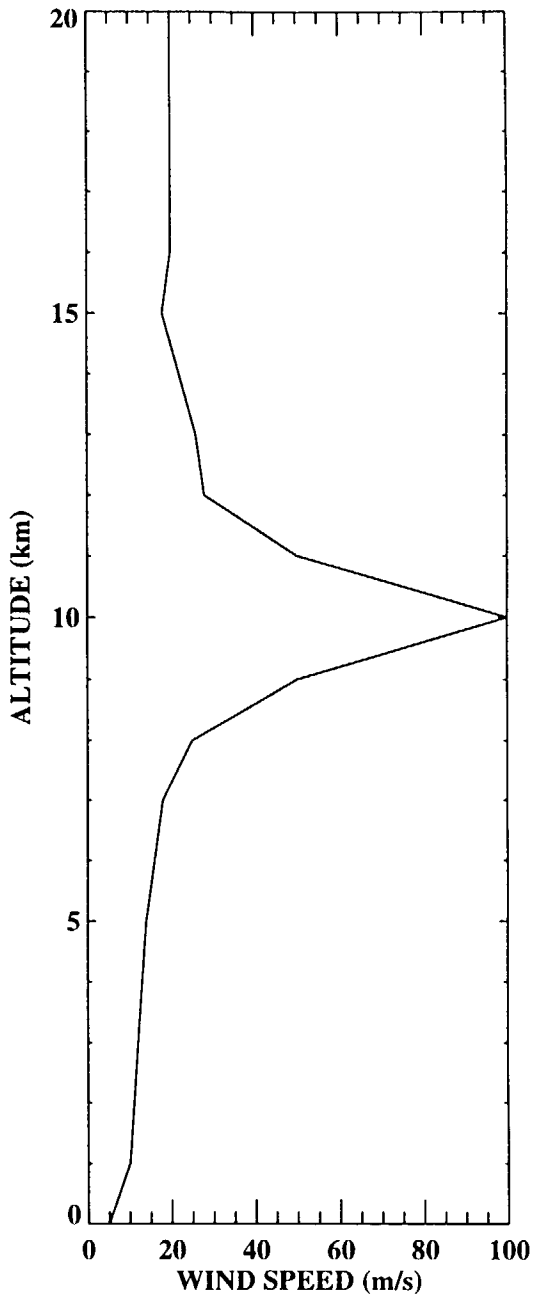
20
15
10
5
0
ALTITUDE (km)
0
20
40
60
80
100
WIND SPEED (m/s)

Fig 4

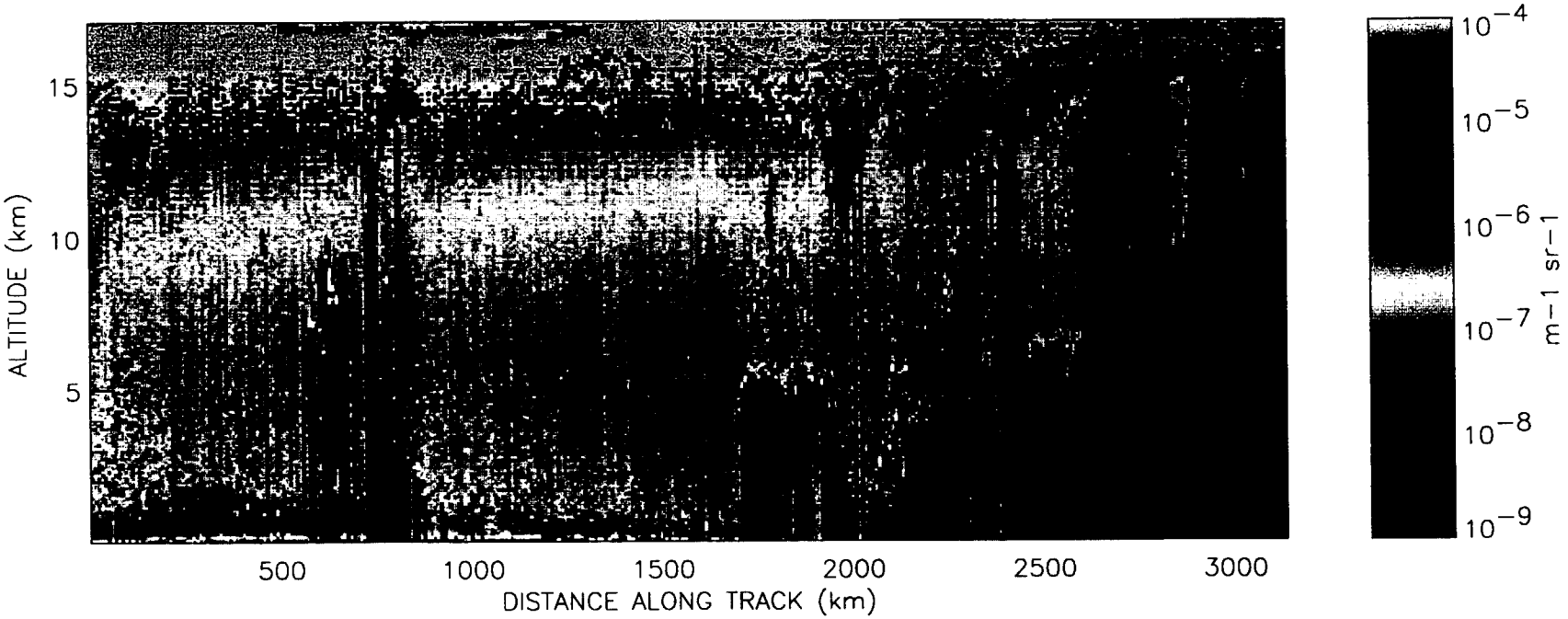
ALTITUDE (km)
15
10
5
500
1000
1500
2000
2500
3000
DISTANCE ALONG TRACK (km)
10^{-4}
10^{-5}
10^{-6}
10^{-7}
10^{-8}
10^{-9}
m−1 sr−1

FIG. 3

a)

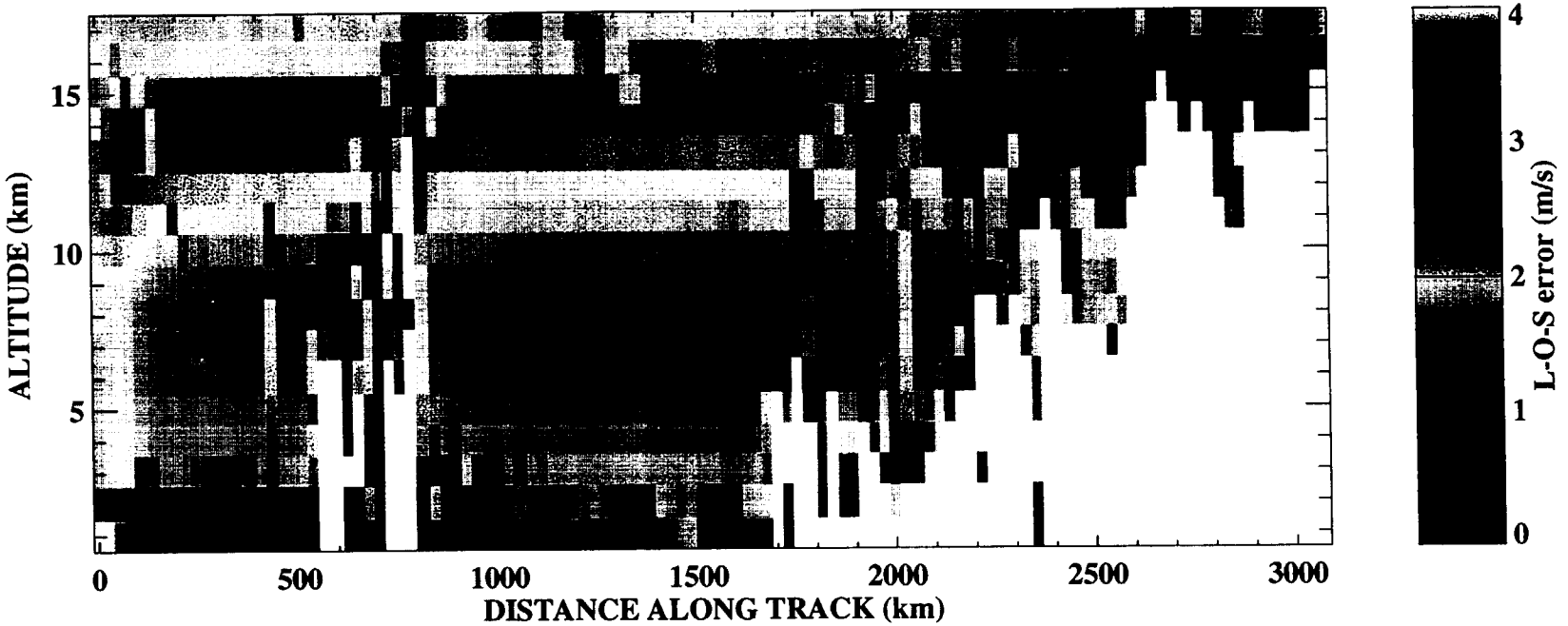
ALTITUDE (km)
15
10
5
0
500
1000
1500
2000
2500
3000
DISTANCE ALONG TRACK (km)
4
3
2
1
0
L-O-S error (m/s)

b)

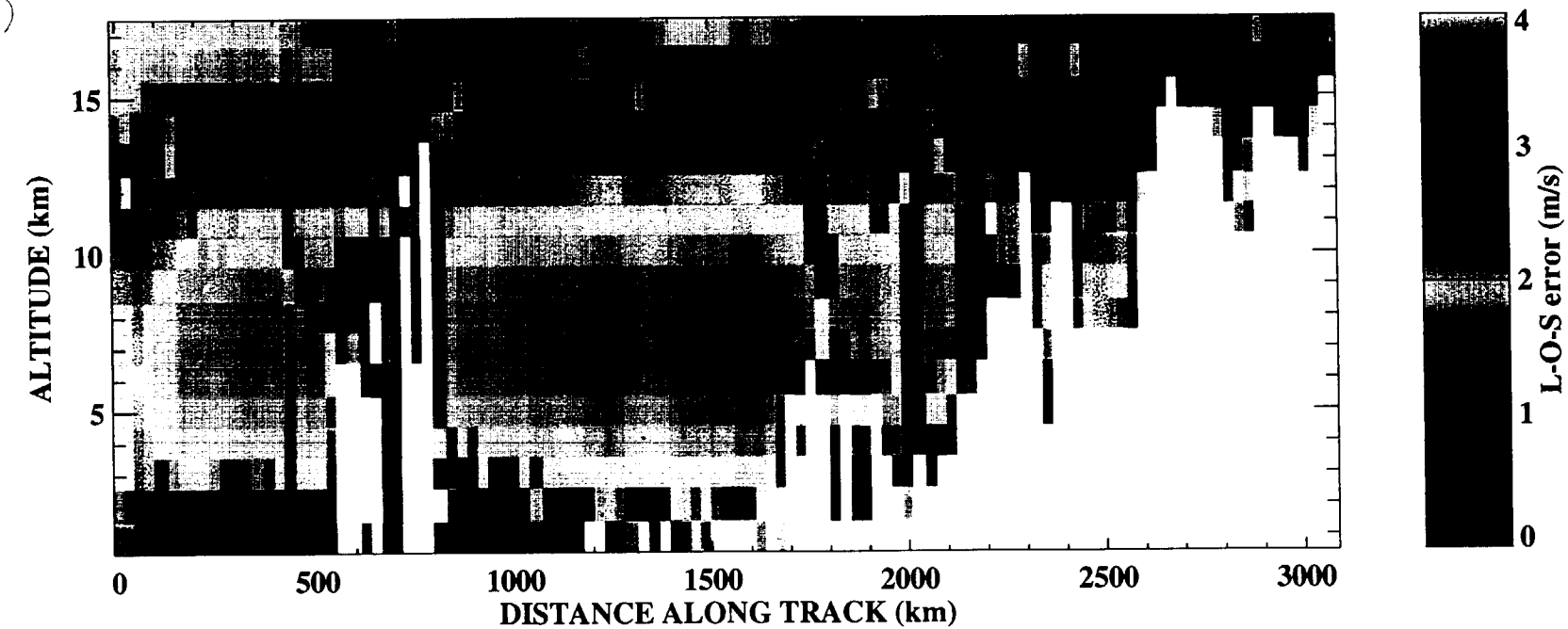
ALTITUDE (km)
15
10
5
0
500
1000
1500
2000
2500
3000
DISTANCE ALONG TRACK (km)
4
3
2
1
0
L-O-S error (m/s)

FIG 5

a)

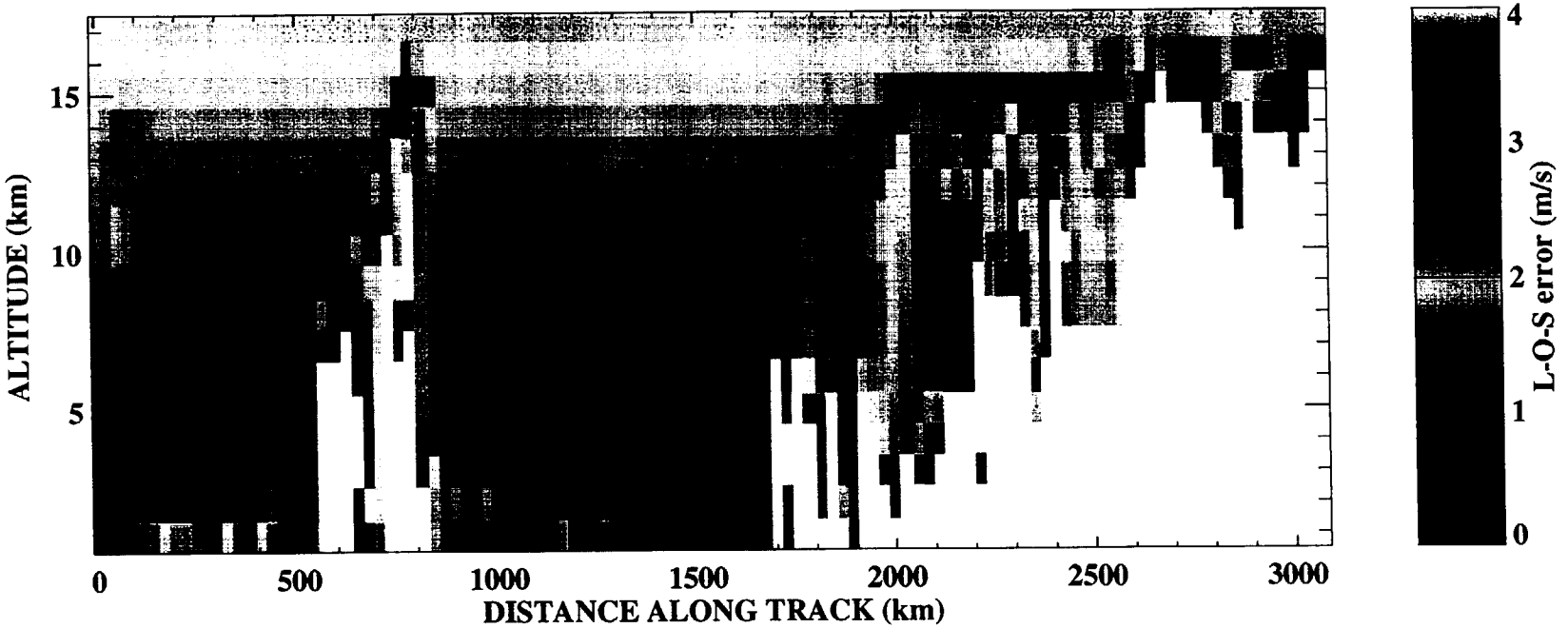
ALTITUDE (km)
15
10
5
0
500
1000
1500
2000
2500
3000
DISTANCE ALONG TRACK (km)
4
3
2
1
0
L-O-S error (m/s)

b)

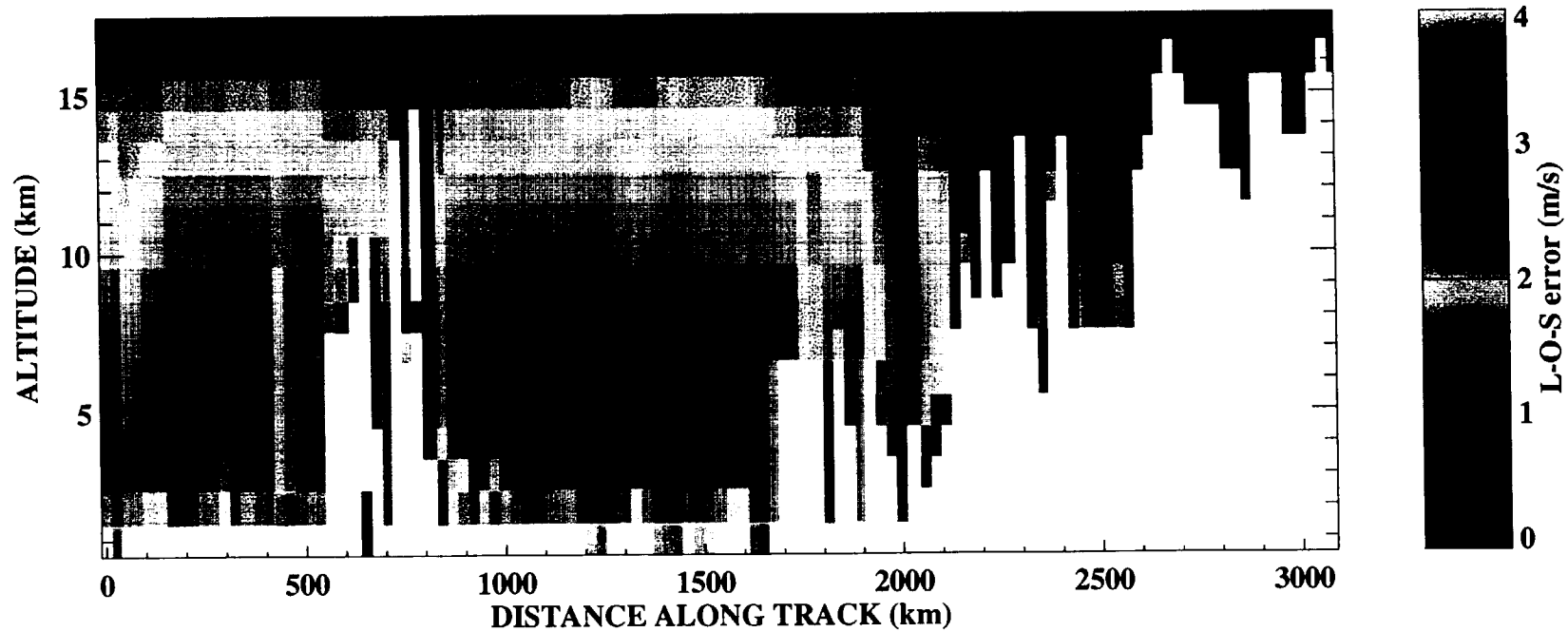
ALTITUDE (km)
15
10
5
0
500
1000
1500
2000
2500
3000
DISTANCE ALONG TRACK (km)
4
3
2
1
0
L-O-S error (m/s)

FIG. 6